



Estimation of 1 km downwelling shortwave radiation over the Tibetan Plateau under all-sky conditions

Peizhen Li¹, Lei Zhong^{1,2,3,4}, Yaoming Ma^{5,6,7,8,9,10}, Yunfei Fu¹, Meilin Cheng¹, Xian Wang¹, Yuting Qi¹, Zixin Wang¹

5 ¹School of Earth and Space Sciences, University of Science and Technology of China, Hefei 230026, China

²CAS Center for Excellence in Comparative Planetology, Hefei 230026, China

³Jiangsu Collaborative Innovation Center for Climate Change, Nanjing 210023, China

10 ⁴Frontiers Science Center for Planetary Exploration and Emerging Technologies, University of Science and Technology of China, Hefei 230026, China

⁵Land-Atmosphere Interaction and its Climatic Effects Group, State Key Laboratory of Tibetan Plateau Earth System, Resources and Environment (TPESRE), Institute of Tibetan Plateau Research, Chinese Academy of Sciences, Beijing 100101, China

15 ⁶College of Earth and Planetary Sciences, University of Chinese Academy of Sciences, Beijing 100049, China

⁷College of Atmospheric Science, Lanzhou University, Lanzhou 730000, China

⁸National Observation and Research Station for Qomolangma Special Atmospheric Processes and Environmental Changes, Dingri 858200, China

⁹Kathmandu Center of Research and Education, Chinese Academy of Sciences, Beijing 100101, China

20 ¹⁰China-Pakistan Joint Research Center on Earth Sciences, Chinese Academy of Sciences, Islamabad 45320, Pakistan

Correspondence to: Lei Zhong (zhonglei@ustc.edu.cn)

Abstract. Downwelling shortwave radiation (DSR) is the basic driving force for the energy and water cycles of the Earth's climate system. As called the Third Pole of the Earth, the Tibetan Plateau (TP) absorbs a large amount of shortwave radiation and exert important impacts on global weather and climate change. However, due to coarse spatial resolution and insufficient consideration of factors influencing radiative transfer processes, DSR parameterization schemes are still need to be improved when applied to the TP. Based on satellite datasets and meteorological forcing data, all-sky DSR over the TP at a spatial resolution of 1 km was derived using an improved parameterization scheme. The influence of topography and different radiative attenuations were comprehensively taken into account. Specifically, the introduction of cloud multiscattering and topography factors further improves the DSR estimation accuracy. The validation results indicated that the developed parameterization scheme showed reasonable accuracy. By comparing with current widely used DSR products based on the same in situ observations, the derived DSR performed much better on different spatial and temporal scales. On

25
30



35 instantaneous, ten-day, and monthly timescales, the root-mean-square errors (RMSEs) of the derived
DSR are 132.8~158.2 W m⁻², 70.8~76.5 W m⁻², and 61.3~67.5 W m⁻², respectively, which are much
smaller than those of current DSR products. The derived DSR not only captured the temporal variation
characteristics that are more consistent with the in situ measurements, but also provided reasonable
spatial patterns. Meanwhile, the proposed parameterization scheme demonstrated its superiority in
40 characterizing more details and high dynamics of the spatial pattern of DSR due to its terrain correction
and high resolution. Moreover, this parameterization scheme does not need any local correction in
advance and it has the potential to be extended to other regions in the world.

1 Introduction

Solar radiation is the basic energy source for surface biological, physical and chemical processes
45 (vegetation photosynthesis, evapotranspiration, plant and crop growth, etc.) (Wang et al., 2015; Liang et
al., 2019). It plays a decisive role in surface energy balance, land–atmosphere interactions, weather and
climate change (Li et al., 1997; Wang and Dickinson, 2013; Huang et al., 2019). Furthermore, it is the
key input data for land surface process models, hydrological models and earth system models (Pinker et
al., 2005; Liang et al., 2010; Stephens et al., 2012; Letu et al., 2020).

50 The Tibetan Plateau (TP) covers an area of approximately 2.65 million square kilometers. It is known
as the "Roof of the World" and "the Third Pole of the Earth" because of its average altitude of more than
4000 m (approximately 1/3 of the troposphere height) and extremely complex topography (Qiu, 2008;
Yao et al., 2012). In addition, the TP and its surrounding areas hold the largest number of glaciers outside
the polar regions (Yao et al., 2012). The Yangtze River, the Yellow River, the Indus River and other major
55 rivers in Asia originate from the TP, and thereby the TP is also called the "Asian Water Tower" (Xu et al.,
2008; Immerzeel et al., 2010). Therefore, the unique features of the TP make it an important research
object of global and regional energy and water circulation and is one of the most sensitive regions in
response to global climate and environmental change.

Due to its high altitude, low air mass and short path for solar radiation to reach its surface, the TP
60 receives a large amount of radiation (Yang et al., 2014; Ma et al., 2017). The analysis of existing
observation data shows that the solar radiation heating effect of the TP is obviously stronger than that of
surrounding areas. Even the measured downwelling shortwave radiation (DSR) exceeds the solar



constant that occurs frequently (Tanaka et al., 2001; Yang et al., 2006b; Yang et al., 2008). As a result, the TP can generate an intense surface heating field, which drives atmospheric circulation, regulates the formation and development of the East Asian monsoon, and exerts an important impact on global weather processes and climate change (Hong et al., 2012; Wu et al., 2012; Zhao et al., 2018; Zhao et al., 2019b). Radiation-related changes to the environment become more severe in the case of global warming, such as significant snow melt, glacier retreat and permafrost thawing (Piao et al., 2010; Yang et al., 2010b; Kuang and Jiao, 2016). In turn, these processes may pose a threat to engineering constructions such as the Qinghai-Tibetan highway and railway (Chen et al., 2006; Yang et al., 2010a). Meanwhile, in the context of carbon neutrality, DSR has become not only a vital source of energy for local residents, but also an indispensable part of photovoltaic energy technologies (Zhang et al., 2017; Huang et al., 2022; Yang et al., 2022). Consequently, reliable DSR estimation over the TP is of great value for many studies and related practical applications.

For many years, in situ measurements, numerical modeling, and satellite remote sensing have been three effective ways to obtain DSR (Liang et al., 2019). In situ measurements are the most direct and reliable way to obtain DSR data with high accuracy and high temporal resolution. However, due to the high maintenance cost of field instruments, DSR observations are available at a smaller number of stations compared to other routine meteorological variables, such as air temperature, pressure and humidity, especially in areas with harsh climate conditions (e.g., Antarctica, the Arctic and the TP). In situ measurements of DSR in these regions are not only sparse but also unevenly distributed. It is therefore not enough to characterize the distribution pattern of DSR at a large spatial scale. Numerical models can provide spatiotemporally continuous DSR data at regional and global scales. However, the spatial resolution is relatively coarse (Decker et al., 2012). The accuracy is limited due to the uncertainties of models in simulating or predicting cloud quantities. In contrast, satellite remote sensing technology has certain advantages in estimating DSR with high spatial resolution over a large spatial coverage. The sensors aboard satellites can dynamically monitor the evolution and spatial distribution of clouds and capture a large amount of information about the atmosphere and underlying surface.

During the past few decades, various satellite-based methods for estimating DSR have been developed, which can be roughly divided into two categories: statistical methods and methods based on radiative transfer processes (Sengupta et al., 2018; Huang et al., 2019; Letu et al., 2020). The statistical



methods used to estimate DSR construct the functional relationship between satellite measurements and in situ observations. Traditional empirical methods are simple to operate by applying statistical regression (Masuda et al., 1995; Li et al., 1997). However, the empirical model may work at the local scale but
95 needs recalibration over different regions. Artificial intelligence models, which can estimate DSR by building nonlinear relationships between satellite signals and ground-based DSR, have become a new trend to estimate radiation flux (Lu et al., 2011; Qin et al., 2011; Wei et al., 2019; Ma et al., 2020a). However, owing to an insufficient physical basis, the calculation accuracy of such methods depends largely on the selection of training data, and consequently, their generalizability is limited. In addition,
100 the artificial intelligence model usually needs a large number of samples to train the model. Therefore, due to insufficient ground-based observations, this method is not easy to apply in the TP (Yang et al., 2010a; Zhang et al., 2015). The look-up table (LUT) and physical parameterization method (Pinker and Laszlo, 1992; Bisht et al., 2005; Liang et al., 2006; Lu et al., 2010; Xie et al., 2016; Tang et al., 2019) are two typical methods based on the radiation transfer process and have been widely used to estimate DSR
105 from satellite data. Since LUT is a close approximation to the complicated radiative transfer model (RTM), a large number of parameters are needed as inputs, such as cloud, aerosol and atmospheric parameters, to obtain higher estimation accuracy. However, the data volume in the LUT will be greatly increased, which will further reduce the estimation efficiency of DSR. At the same time, it is usually necessary to encrypt the discrete calculation results by means of complex interpolation algorithms (Letu et al., 2020), which in turn will lead to a computational load. Alternatively, the physical parameterization
110 method can alleviate the computational burden by parameterizing the complex process in RTM while maintaining sufficient estimation accuracy.

To date, the DSR parameterization scheme under clear-sky conditions has been quite mature (Bisht et al., 2005; Gueymard, 2012; Hwang et al., 2012). However, since optical remote sensing is greatly
115 affected by clouds, it is still a problem to be solved to estimate DSR efficiently and accurately under all-sky conditions (Li et al., 1995; Li et al., 1997). Although some studies have proposed parameterization schemes for cloudy-sky conditions, the current schemes still have some defects. In the presence of clouds, cloud-sky parameterization, which only considers cloud fraction and cloud optical thickness, is usually coupled into clear-sky models in a simple and arbitrary manner (Niemela et al., 2001; Bisht and Bras,
120 2010). Second, many parameterization schemes do not consider the DSR attenuation caused by clouds



carefully enough. Generally, only the single scattering of clouds is considered, and the multiple scattering effect of clouds is ignored.

Due to the high elevation and complex terrain of the TP, the impact of terrain on DSR should be taken into account. Tovar et al. (1995) found that there is no obvious correlation between the spatial variation in radiation in mountainous areas and interstation distance, but it varies with the altitude difference. Therefore, the DSR in mountainous areas cannot be estimated simply by interpolation of adjacent observation values. Yang et al. (2006b) pointed out that GEWEX-SRB v2.5 greatly underestimated the DSR on the TP due to ignoring the influence of surface elevation. Olson and Rupper (2019) reported that the deviation of the surface radiation budget could exceed 40 W m^{-2} during the summer melting season in the high-mountain Asia area. In addition, the coarse spatial resolution of most existing DSR products is prone to cause uncertainties in rugged areas such as the TP. Currently, the spatial resolution and accuracy of most existing DSR products cannot meet the requirements of energy and water cycle studies over the TP (Zhong et al., 2019a; Wang et al., 2021; Zhang et al., 2022). Therefore, all-sky DSR products with fine spatial resolution and high accuracy over the TP are still lacking.

In general, some existing DSR estimation methods are still not applicable to the TP due to its highly variable terrain, high elevation, and unique climatic conditions. Therefore, an effective method to estimate the DSR of the entire TP under all-sky conditions is urgently needed. In this study, an improved parameterization scheme is proposed, and the derived DSR is validated by in situ measurements and compared with various existing DSR products. Then, the spatiotemporal distribution of the estimated DSR is presented, and the improvement brought by considering the multiple scattering effect of clouds and topographic factors is discussed. The paper is organized as follows: Section 2 introduces the input data and validation data. Section 3 introduces the improved parameterization method. Section 4 presents the results and discussion. The main conclusions are given in Section 5.

2 Data

2.1 Input data

The basic information of the meteorological forcing data and satellite datasets are listed in Table 1. The China Meteorological Forcing Dataset (CMFD) has a temporal resolution of 3 hours and a horizontal spatial resolution of 0.1° . It has been widely used by the scientific community due to its high resolution



and quality. These forcing data were produced by combining routine meteorological observations of the
150 China Meteorological Administration (CMA), Princeton reanalysis datasets, the Global Land Data
Assimilation System (GLDAS), the GEWEX Surface Radiation Budget (GEWEX-SRB) and the Tropical
Rainfall Measuring Mission (TRMM) satellite (He et al., 2020). The surface air pressure (Pa), air
temperature (K) and specific humidity (kg kg^{-1}) are used for DSR estimation.

The satellite data come from MODIS, OMI and ASTER. The inputs for the parameterization scheme
155 include (1) the cloud phase, cloud water path (CWP), cloud effective radius (CER) (MODIS cloud
product MOD06_L2), (2) aerosol optical depth (AOD) (MODIS aerosol products MOD04_L2), (3)
ground surface albedo (MODIS Combined Land Albedo Product MCD43C3), (4) geolocation
information (MOD03), (5) total ozone column amount (OMTO3e), and (6) 30-m ASTER digital
elevation model.

160 The MODIS combined Dark Target and Deep Blue AOD at $0.55 \mu\text{m}$ for land and ocean were used
to derive the aerosol Ångström turbidity coefficients (Yang et al., 2006a; Tang et al., 2019). The actual
surface albedo is derived with the shortwave black sky albedo (BSA) and white sky albedo (WSA) from
the albedo product (Schaaf et al., 2002; Pinty et al., 2005). All MODIS product versions mentioned above
are in collection 6. The OMI science team created the OMTO3e product by selecting the best pixel data
165 from the high-quality filtered level-2 total column ozone data (Ahn et al., 2008).

It should be noted that in operational applications, many parameters may not be available, especially
in areas with extreme climatic conditions, such as the TP. Therefore, the "gap-filling" procedure should
be carried out first, as in most studies. For aerosols, the invalid retrievals would be substituted using the
Level-3 MODIS global daily and monthly climatological products (Qin et al., 2015; Huang et al., 2016a;
170 Li et al., 2022). For the ozone column amount and surface albedo, the unavailable retrievals were
substituted using the nearest valid retrievals (Huang et al., 2018; Tang et al., 2019; Zhong et al., 2019b).
The spatial resolutions of MODIS aerosol and albedo data are 10 km and 5 km, respectively. The spatial
resolutions of ozone and DEM data are 25 km and 30 m, respectively. To obtain the DSR at the 1 km
spatial scale, these data were resampled to 1 km.

175 **Table 1.** Overview of the meteorological forcing and satellite datasets used in this study.

Data sources	Product name	Variable	Spatial resolution	Temporal extent
--------------	--------------	----------	--------------------	-----------------



CMFD	-	Temperature	0.1° x 0.1°	1979 to 2018	
		Pressure			
		Specific humidity			
		Cloud phase			
		Cloud water path			1 km
MODIS	MOD06_L2	Cloud effective radius	10 km	2000 to present	
	MOD04_L2	Aerosol optical depth			
	MCD43C3	Black-Sky albedo			5 km
		White-Sky albedo			
	MOD03	Latitude			1 km
ASTER	AST14DEM	Longitude	30 m	2000 to present	
		Solar zenith			
OMI	OMTO3e	DEM	0.25° x 0.25°	2004 to present	

2.2 In situ observation stations

The distributions of the in situ observation stations are marked in Fig. 1, and their basic information is listed in Table 2. In this study, in situ DSR observations used to validate the accuracy of the improved parameterization scheme were extracted from 12 stations over the TP. A variety of elevations, climates, and land cover types are included in these validation stations. Among them, six stations are obtained from the Tibetan Observation and Research Platform (TORP) project (Ma et al., 2008), including BJ, QOMS, SETORS, NADORS, MAWORS and NAMORS stations. These six stations composed an integrated high-elevation and cold-region observation network. More detailed descriptions of these six stations are described by Ma et al. (2020b). The Xidatan (XDT) monitoring station representing the characteristics of discontinuous and warm permafrost is located along the northern permafrost boundary of the TP. The Tanggula (TGL) monitoring station is located in the hinterland of the TP and is characterized by a continuous and cold permafrost zone (Yao et al., 2011; Zhao et al., 2021). There are two stations in the Ngoring Lake basin, which is located in the Yellow River source area east of the TP (Li et al., 2017). One grassland station (NLGS) is located on a flat surface, and the other observation station (NLTS) is located on the lakeside beside the lakeshore tower station (Li et al., 2020; Li et al., 2021). The in situ data of D105 and NPAM come from the Coordinated Enhanced Observing Period Asia-Australia Monsoon Project (CAMP) on the Tibetan Plateau (CAMP/Tibet) (Ma et al., 2009; Zhong et al., 2010; Ma et al., 2014).



195 **Table 2.** Basic information for the in situ observation stations over the Tibetan Plateau.

Site	Lat(°N)	Lon(°E)	Altitude(m)	Land cover	Instrument	Frequency
BJ	31.37	91.90	4509	Alpine meadow	CM21, Kipp & Zonen	1 h
D105	33.06	91.93	5039	Alpine sparse grassland	CM21, Kipp & Zonen	1 h
NPAM	31.93	91.71	4620	Alpine meadow and grassy marshland	CM21, Kipp & Zonen	1 h
QOMS	28.36	86.95	4298	Gravel and sparse meadow	CNR1, Kipp & Zonen	1 h
SETORS	29.77	94.73	3327	Alpine meadow	CNR1, Kipp & Zonen	1 h
MAWORS	38.41	75.05	3668	Alpine desert	NR01, Kipp & Zonen	1 h
NADORS	33.39	79.70	4270	Alpine desert	NR01, Kipp & Zonen	1 h
NAMORS	30.77	90.98	4730	Alpine steppe	NR01, Vaisala	1 h
NLGS	34.91	97.55	4280	Flat Grassland	CNR4, Kipp & Zonen	0.5 h
NLTS	34.91	97.57	4275	Water	CNR4, Kipp & Zonen	0.5 h
XDT	35.72	94.13	4538	Alpine meadow	CM3, Kipp & Zonen	0.5 h
TGL	33.07	91.94	5100	Alpine sparse meadow	CM3, Kipp & Zonen	0.5 h

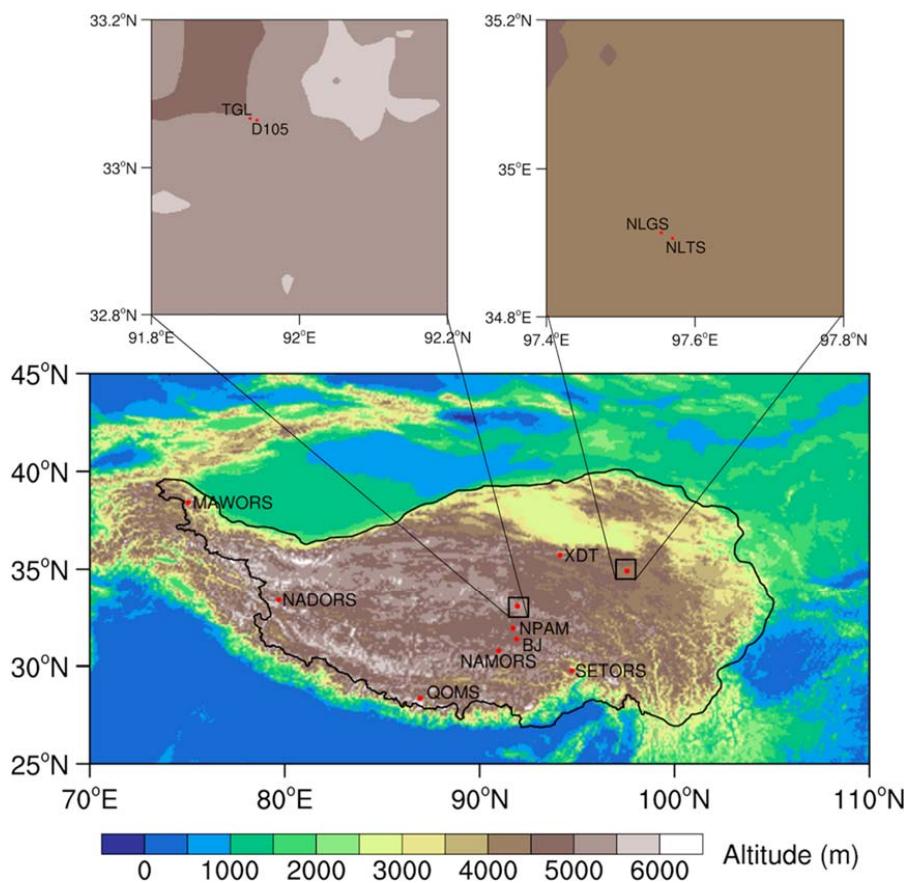


Figure 1. Locations of the twelve in situ observation stations over the TP.

3 Methodology

- 200 The effects caused by ozone, aerosol, water vapor, Rayleigh scattering, permanent gases, clouds and terrain are comprehensively taken into account in the improved parameterization scheme. More importantly, the DSR varies with altitude, surface slope and aspect, and the multiple actions of cloud and topography factors on DSR have been neglected in many previous studies. The all-sky DSR estimation method is divided into two groups, one for clear-sky conditions and the other for cloudy-sky conditions.
- 205 The main steps of the method and related key variables are shown in Fig. 2.

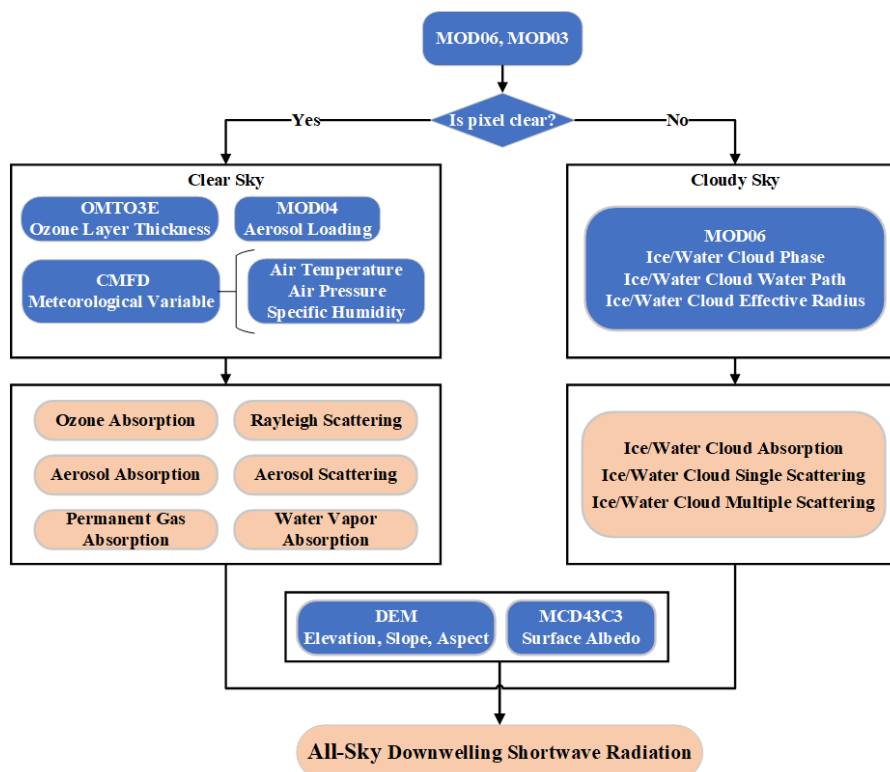


Figure 2. Flowchart for estimating all-sky DSR.

3.1 Clear-Sky Scheme

The DSR under clear-sky conditions (DSR_{ctr}) can be calculated as the sum of three components: direct
 210 (beam) radiation ($S_{b,ctr}$), diffuse radiation ($S_{d,ctr}$), and reflected insolation from the surrounding terrain
 ($S_{r,ctr}$).

$$DSR_{ctr} = S_{b,ctr} + S_{d,ctr} + S_{r,ctr} = S_0(\tau_{b,ctr} + \tau_{d,ctr} + \tau_{r,ctr}), \quad (1)$$

where S_0 denotes the horizontal extraterrestrial solar insolation, which may slightly change with the
 earth-sun distance throughout the year. In addition, $\tau_{b,ctr}$ is the direct radiative transmittance; $\tau_{d,ctr}$ is
 215 the diffuse radiative transmittance; and $\tau_{r,ctr}$ is the reflectance radiative transmittance.

3.2 Cloud-Sky Scheme

DSR under cloudy-sky conditions (DSR_{cld}) can be divided into four items as follows:

$$DSR_{cld} = S_{b,cld} + S_{d,cld} + S_{am,cld} + S_{r,cld}$$



$$= S_0 \tau_{b,cld} + S_0 \tau_{d,cld} + S_0 (\tau_{b,cld} + \tau_{d,cld}) \frac{\rho_{a,cld} \rho_g}{1 - \rho_{a,cld} \rho_g} + S_0 \tau_{r,cld}, \quad (2)$$

220 where the first, second and fourth items are the direct solar irradiance ($S_{b,cld}$), diffuse solar irradiance
($S_{d,cld}$), and reflected solar irradiance ($S_{r,cld}$) under cloudy conditions, respectively. The third item is the
ambient solar irradiance caused by the interactions between the surface and atmosphere ($S_{am,cld}$). $\tau_{b,cld}$
is the direct radiative transmittance; $\tau_{d,cld}$ is the diffuse radiative transmittance; $\tau_{r,cld}$ is the
reflectance radiative transmittance; and $\rho_{a,cld}$ is the atmosphere hemispherical albedo under cloudy-sky
225 conditions. ρ_g is the ground surface albedo.

The variations in elevation, slope and aspect of the land surface are considered for the above radiative
transmittance. A detailed description of $\tau_{b,ctr}$, $\tau_{d,ctr}$, $\tau_{r,ctr}$, $\tau_{b,cld}$, $\tau_{d,cld}$, $\tau_{r,cld}$, $\rho_{a,cld}$ and ρ_g is
presented in Appendix A.

4 Results and Discussions

230 Considering the integrity and temporal continuity of the available data, the data of the BJ, D105, NPAM
and SETORS stations in 2008, the data of the QOMS station in 2008 and 2015, and the data of the
remaining seven stations in 2015 are used for validation. To ensure the reliability of the validation, first,
the outliers in the ground-based observations were removed by considering the valid range and time
continuity. Then, the hourly data were smoothed to 30 minutes to match the satellite overpass time and
235 the station observation time (Huang et al., 2016b). The root-mean-square error (RMSE), mean bias (MB),
mean absolute error (MAE) and Pearson correlation coefficient (R) are used to evaluate the performance
of the radiation parameterization scheme.

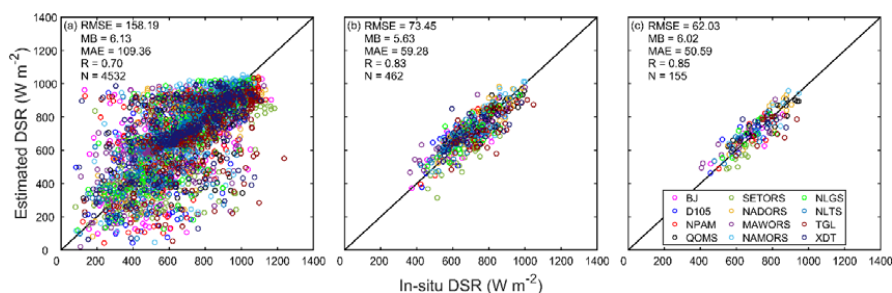
4.1 Validation against in situ measurements

As shown in Fig. 3a, the RMSE and R of the 1 km all-sky DSR are 158.19 W m⁻² and 0.70 at an
240 instantaneous timescale, respectively. Although the validation results of this study are worse than those
of other plain areas (RMSE and R were usually approximately 100 W m⁻² and 0.9, respectively),
considering the unique climate characteristics of the TP and compared with the existing DSR products
and algorithms (see Section 4.2 and Section 4.4 for details), the accuracy of the results is within an
acceptable range. Roupioz et al. (2016) estimated all-sky solar radiation at an instantaneous timescale
245 based on MODIS products, but the retrievals were validated using only BJ, QOMS and NAMORS



stations. In their study, the RMSE, MB and R of BJ station were 225.5 W m^{-2} , 120.1 W m^{-2} and 0.51, respectively; the RMSE, MB and R of QOMS station were 117.1 W m^{-2} , 13.0 W m^{-2} and 0.74, respectively; and the RMSE, MB and R of NAMORS station were 203.5 W m^{-2} , 39.5 W m^{-2} and 0.55, respectively. Table 3 shows that the accuracy of our DSR estimation is better than Roupioz's retrievals.

250 Representativeness errors of point-scale measurements can affect the validation results of instantaneous DSR estimations to some extent. The insufficient spatial representation of point-scale observations can be partly compensated by lowering their temporal resolution (Hakuba et al., 2013; Huang et al., 2016b). Therefore, the DSR estimation results were also validated at ten-day and monthly timescales. There are three 10-day periods within 1 month, which can be defined as follows: from the
255 first to the 10th, from the 11th to the 20th, and from the 21st to the end of every month. Obviously, the estimation of DSR at a longer timescale shows more reasonable agreement with the in situ measurements compared with the instantaneous DSR estimations (Fig. 3b and Fig. 3c).



260 **Figure 3.** Validation results for the estimated all-sky DSR on different time scales ((a) instantaneous scale; (b) ten-day scale; (c) monthly scale). N indicates the number of points. The legend with different colors denotes the twelve stations involved in the validation. The units of RMSE, MB and MAE are W m^{-2} .

The corresponding statistical indices for the twelve stations in this study are listed in Table 3. Since there is usually a distinctness between DSR estimation under clear-sky and cloudy-sky conditions, the statistics of specific stations are always related to the overall cloud fraction. Therefore, the proportion of
265 cloud cover days (CCD) at each station is also listed in the table. Zhong et al. (2019b) estimated all-sky solar radiation on a ten-day timescale based on MODIS products over the TP, while their method needed to obtain ground-based measurements in advance for local calibration. We find that compared to the statistics presented at the D105, QOMS, and SETORS stations, the accuracies of our method are on average slightly higher.

270 As illustrated in Table 3, the best validation results occurred at the QOMS station, showing the



lowest RMSE, the MB of a smaller absolute value, and the higher R, due to the extremely low CCD over there (~19.83%), whereas the poorer performance occurred at the SETORS and TGL stations, according to the validation results on various time scales. The SETORS station is located in the valley near the southeastern TP, surrounded by dense vegetation (mainly evergreen needle-leaved trees and alpine meadows) and is close to the southern water vapor transport channel. Accordingly, many precipitation events occur here, with a maximum CCD (~72.85%) among the twelve sites. The TGL station lies on the north side of the Tanggula Mountains, surrounded by numerous glaciers and deep snow cover, which can persist for many days (Xu et al., 2017; Zhou et al., 2018). Because the snow/ice cover beneath the clouds is difficult to identify from satellite signals, there is great uncertainty in the corresponding retrievals of cloud microphysical parameters, which may lead to low accuracy of the estimation results. In addition, previous studies have shown that snow cover will result in the underestimation of DSR (Pinker et al., 2007; Huang et al., 2016a), which is also indicated by the large negative MB of the TGL site compared with other stations.

Table 3. Summary statistics of the validation results for each station on different timescales.

Site	Instantaneous timescale			Ten-day timescale			Monthly timescale			CCD
	RMSE (W m ⁻²)	MB (W m ⁻²)	R	RMSE (W m ⁻²)	MB (W m ⁻²)	R	RMSE (W m ⁻²)	MB (W m ⁻²)	R	
BJ	179.44	11.41	0.66	66.20	13.91	0.84	56.01	14.54	0.81	49.58%
D105	162.87	32.47	0.67	76.69	33.23	0.73	67.43	33.80	0.73	54.02%
NPAM	177.57	-3.90	0.63	67.63	-4.28	0.82	51.90	-3.75	0.82	53.46%
QOMS	112.33	5.04	0.74	56.49	6.38	0.90	49.76	6.41	0.91	19.83%
SETORS	183.33	-49.51	0.67	94.17	-49.48	0.67	64.89	-44.04	0.74	72.85%
MAWORS	167.41	28.51	0.71	83.27	27.08	0.90	72.94	27.32	0.92	55.62%
NADORS	129.88	19.48	0.78	66.20	17.59	0.89	58.30	18.20	0.90	35.07%
NAMORS	150.62	18.30	0.72	65.60	13.66	0.88	55.92	13.42	0.89	40.27%
NLGS	141.53	11.26	0.77	66.51	10.81	0.81	56.48	11.02	0.80	46.58%
NLTS	136.29	24.63	0.79	62.80	22.01	0.86	51.55	23.81	0.87	59.45%
XDT	183.08	17.84	0.63	81.41	17.95	0.72	70.48	18.02	0.70	51.23%
TGL	188.98	-46.64	0.58	97.70	-46.52	0.72	87.80	-46.92	0.66	45.63%

285

4.2 Comparison among different DSR products

To further evaluate the reliability of our DSR estimates, several existing widely used DSR products were selected for comparison based on the same in situ observations used in Section 4.1. Among these products,



there are remotely sensed and reanalysis DSR products, namely, Clouds and the Earth’s Radiant Energy
 290 System Synoptic (CERES_SYN) surface fluxes (Loeb et al., 2013), Global Energy and Water Exchanges
 Surface Radiation Budget (GEWEX_SRB) datasets (Zhang et al., 2014) and the fifth generation
 reanalysis (ERA5) from the European Centre for Medium-Range Weather Forecasts (ECMWF) (Hans et
 al., 2019). As mentioned in Section 2, CMFD is meteorological forcing data, which also contains the
 DSR variable and is also selected for intercomparison in our study. In addition, Tang et al. (2019)
 295 produced a high-resolution (10 km, 3H) DSR dataset (short for “Tang_ISCCP” in our study) based on
 the latest International Satellite Cloud Climatology Project (ISCCP) HXG cloud products, which were
 also selected for comparison.

It is known that spatial mismatch may incur errors in the validation results, so our results at the
 original scale of 1 km were aggregated to the corresponding spatial resolution of the above products. The
 300 temporal resolution of the GEWEX_SRB, CMFD and Tang_ISCCP products is 3 hours, while that of
 ERA5 is 1 hour. CERES_SYN products have two time resolutions of 1 hour and 3 hours. The
 abovementioned DSR products and the estimated DSR of this study were temporally matched to 10:30
 local time for mutual comparison (Zhong et al., 2019b).

Table 4. Comparison with existing DSR products on different timescales in terms of accuracy.

Product name	Instantaneous timescale			Ten-day timescale			Monthly timescale			Spatial resolution
	RMSE ($W m^{-2}$)	MB ($W m^{-2}$)	R	RMSE ($W m^{-2}$)	MB ($W m^{-2}$)	R	RMSE ($W m^{-2}$)	MB ($W m^{-2}$)	R	
This study	158.19	6.13	0.70	73.45	5.63	0.83	62.03	6.02	0.85	1 km
CMFD	179.50	-74.42	0.67	108.29	-75.47	0.85	96.41	-74.98	0.89	
Tang_ISCCP	186.26	-65.35	0.67	109.85	-66.07	0.81	97.08	-65.63	0.85	10 km
This study	140.77	14.67	0.75	76.51	14.59	0.82	67.55	15.11	0.83	
ERA5	165.67	-20.59	0.65	88.06	-21.44	0.82	74.19	-21.06	0.86	25 km
This study	135.11	15.67	0.77	75.01	15.24	0.83	67.12	15.75	0.83	
CERES_SYN_1h	146.64	-46.70	0.75	84.27	-47.93	0.86	73.25	-47.53	0.89	
CERES_SYN_3h	160.50	-78.30	0.74	107.13	-79.48	0.85	98.67	-79.06	0.88	100 km
GEWEX_SRB	194.45	-118.56	0.68	143.68	-119.71	0.80	135.54	-119.21	0.83	
This study	132.84	2.79	0.77	70.84	2.18	0.84	61.33	2.70	0.85	

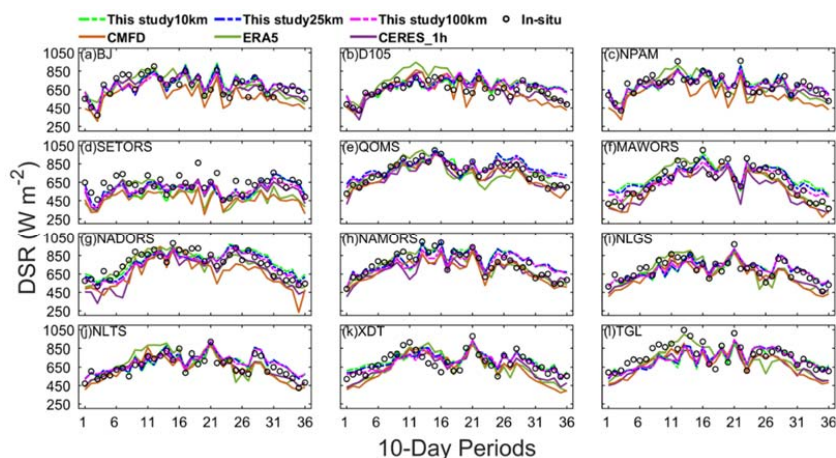
305

As summarized in Table 4, the RMSE range of the DSR products is approximately 150~190 $W m^{-2}$
 on the instantaneous scale; on the ten-day scale, their RMSE range is approximately 80~140 $W m^{-2}$, and
 their RMSE range is approximately 70~130 $W m^{-2}$ on the monthly scale. The MB range of DSR products



is $-120 \sim -20 \text{ W m}^{-2}$ on three time scales. These large spans of RMSE and MB indicate that the current
310 DSR products still have great uncertainties over the TP. The estimates of this study have the smallest
RMSE, the lowest absolute value MB and comparable R values on the corresponding spatial and temporal
scales compared with the existing products. This means that the derived DSR based on the proposed
method performs better than the current DSR products over the TP.

In addition, it is noted that the accuracies of all datasets have been appreciably improved with
315 increasing timescale. This is because the 3D radiative transfer effects and complexity of clouds can be
significantly reduced and the spatial representativeness of ground-based measurements can be
significantly enhanced through temporal averaging (Huang et al., 2016b; Huang et al., 2016a). A
phenomenon in which the RMSE of this study has been improved on an instantaneous scale with
incremental space scales is also found. However, at the ten-day and monthly scales, only the RMSE at
320 the 100 km spatial scale improved, and the variations were relatively small. This may be because the
time mismatch between satellite observations and surface measurements can be partly decreased by
inherent averaging in the upscaling of spatial resolution (Tang et al., 2019).



325 **Figure 4.** Intercomparison of time series of DSR among CMFD, ERA5, CERES_SYN_1 h, and this study at (a) BJ, (b) DT05, (c) NPAM, (d) SETORS, (e) QOMS, (f) MAWORS, (g) NADORS, (h) NAMORS, (i) NLGS, (j) NLTS, (k) XDT, and (l) TGL stations on a ten-day timescale. The circle denotes in situ data.

DSR products with relatively high accuracy, which correspond to three spatial resolutions of 10
km, 25 km and 100 km, are selected for comparison with the estimated DSR in this study in terms of
temporal variation characteristics (Fig. 4). It can be seen that six selected DSR showed a quasi-convex



330 shape in one year at all stations except SETORS. There are some fluctuations in DSR during the summer
monsoon period due to the high frequency of clouds and precipitation. Almost all six selected DSRs
showed relatively smooth variation at SETORS compared with other stations, which demonstrated a large
variation with time. The dynamic range (defined as the difference between the maximum and the
minimum in a year) of CMFD is the largest, while ERA5, CERES_SYN_1 h and this study show similar
335 dynamic ranges. Compared with other products, the derived DSR of this study is more consistent with
the in situ observations at each station, and all show similar temporal change trends.

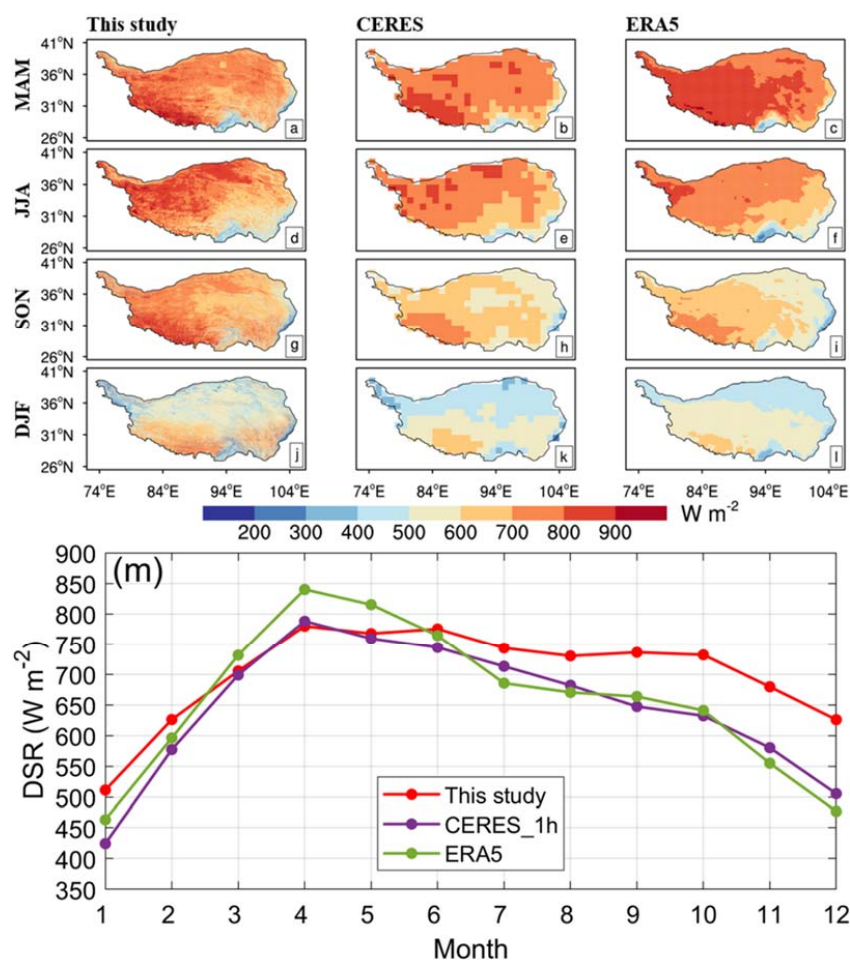
It should be noted that the six selected DSRs are not consistent with the in situ observations at the
SETORS station, especially in the monsoon period in which obvious underestimation can be found.
Cloud and precipitation occurrence frequencies generally reach peaks during the monsoon period over
340 the TP. Compared with other regions of the TP, not only higher cloud amounts and frequencies but also
higher precipitation intensities and frequencies are found in the southeastern TP, where the SETORS
station is located (Zhao et al., 2019a; Kukulies et al., 2020). Convective clouds appear most frequently
over the TP near noon, and thus, the DSR may also partially come from the high diffuse radiation caused
by cloud scattering in addition to direct radiation (Fujinami et al., 2005; Li et al., 2008; Yang et al., 2010a).
345 It is still difficult to reflect the 3D radiation effect of clouds, although this study has considered the
scattering of clouds and thus may lead to underestimation of DSR. The microphysical processes of
convective clouds generally include mixed-phase processes inside clouds (Fu et al., 2020). Nevertheless,
only a single phase can be diagnosed by satellite-based cloud products, which may significantly influence
the retrieval accuracy of DSR (Platnick et al., 2003; Platnick et al., 2017). In addition, the SETORS
350 station is flat with grass cover, while its surroundings are valley and dense evergreen needle-leaved trees.
The domes of instruments are vulnerable to the contamination of precipitation, and further influence the
spatial representativeness of in situ stations. Hence, some errors may be introduced due to the inadequate
spatial representativeness of point-scale measurements compared with the coarse resolution of satellite
images.

355 4.3 Spatiotemporal variations in surface downward shortwave radiation

Based on the above analysis, CERES_SYN_1 h and ERA5 performed better than the other DSR products.
To better investigate the spatiotemporal variations in the estimated DSR over the TP, the seasonal spatial
distribution of DSR generated from CERES_SYN_1 h, ERA5 and this study in 2008 are collected and



compared in Fig. 5. In general, the three mentioned DSR provide similar seasonal radiation patterns, i.e.,
 360 the DSR values are higher in spring and summer and lower in autumn and winter. This phenomenon can
 also be found in the monthly mean DSR variation over the TP (Fig. 5m). The DSR increased from a
 minimum value in January to a maximum value in April. The formation of this pattern is primarily
 controlled by the north-south movement of the subsolar point.



365 **Figure 5.** Spatial distribution of DSR from this study (left), CERES_SYN_1 h (center), and ERA5 (right) for four
 seasons in 2008 over the TP. The first to fourth rows represent spring (March, April and May), summer (June, July
 and August), autumn (September, October and November), and winter (December, January and February),
 respectively. The bottom panel (m) shows the comparison of monthly temporal variation of spatial mean DSR
 estimates from this study, CERES_SYN_1 h, and ERA5 over the TP.

370 It should be pointed out that the radiation texture of this study is rather clear due to the higher



375 resolution (1 km), and more details of DSR variations can be captured. The high values of DSR are mostly located in the western TP. This can be explained by the fact that the western TP, with arid and semiarid climate characteristics, has a higher altitude than the eastern TP, and thus, less radiation attenuation occurred. At the same time, the southern margin of the TP and the eastern margin of the TP near the Sichuan Basin are always low-value areas of DSR. The south edge of the TP is a water vapor transport channel associated with the South Asian monsoon, and the frequencies of clouds and rainfall are high. The eastern edge of the TP near the Sichuan Basin has a very low altitude (~ 1800 m) and is often covered by stratiform clouds. Accordingly, strong solar radiation attenuation occurred in these two regions.

380 The difference among the three mentioned DSRs is also displayed in Fig. 5. The high value of DSR appears in the southwestern TP in spring, but the high value of ERA5 covers a large area and even extends to the Tanggula Mountains (Fig. 5a-c). The overall DSR pattern over the TP shows a decreasing trend from northwest to southeast in summer, but the high value in the Qaidam Basin is not found in ERA5 (Fig. 5d-f). In autumn, the high value of DSR is concentrated in the southwestern TP, showing a spatial pattern of high-west and low-east (Fig. 5g-i). In winter, the DSR reaches the minimum of the year and shows a spatial distribution of high-south and low-north over the TP (Fig. 5j-l). However, the DSR derived from this study is generally higher than that of the other two products. The monthly temporal variation in the spatial mean DSR over the TP also indicates a similar phenomenon (Fig. 5m). The spatial mean DSR of ERA5 is higher than those of the other two DSR products in spring, and the spatial mean
 385
 390 DSR estimated in this study is higher than those of the other two radiation products in autumn and winter.

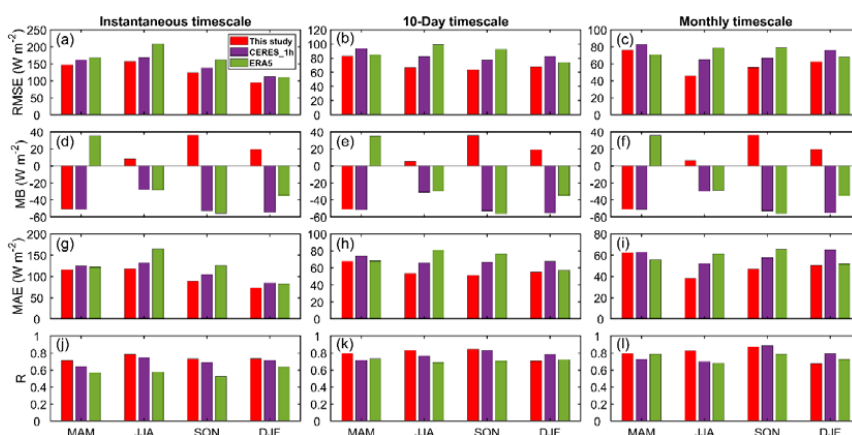


Figure 6. RMSE (a-c), MB (d-f), MAE (g-i) and R (j-l) between in situ observations and DSR estimates from this



study (red bar), CERES_SYN_1 h (purple bar), and ERA5 (green bar) products in four seasons.

To further understand the difference between the three mentioned DSRs, the corresponding
395 statistical indices for the four seasons are presented in Fig. 6. At all temporal scales in spring, ERA5
shows a positive bias, while the other two DSRs show a negative bias. In summer, autumn and winter,
the DSR estimated from this study shows positive bias, while the other two products show negative bias.
This explains the above phenomenon. However, this study is significantly lower than the other two DSR
products in terms of the absolute value of MB. Particularly, it can be clearly seen that in all seasons and
400 temporal scales, not only in MB but also in terms of RMSE and MAE, this study shows the lowest values,
and in terms of R, this study is comparable to or higher than the CERES_SYN_1 h and ERA5 products.
Similar comparison and verification results can also be found in Table 4. In addition, the spatial
distribution of this study is similar to that in a previous study by Zhong et al. (2019b). Therefore, it is not
difficult to conclude from the above analysis that the DSR patterns of this study are reasonable enough,
405 at least showing advantages over other products in terms of spatial resolution with relevant details.

4.4 Evaluation of cloud multiscattering and topographic effects

To evaluate the effects of cloud multiscattering and complex topography, the accuracy of the DSR derived
with and without considering terrain factors and cloud multiple scattering on different temporal scales
were compared (Table 5). Here, four simple cases were designed. Both terrain factor and cloud multiple
410 scattering are not included in Case 1; Case 2 only considers terrain factor, and Case 3 only considers
cloud multiple scattering. Case 4 is the method adopted in this study; that is, both terrain factor and cloud
multiple scattering are taken into account.

Table 5. Comparison between DSR estimation with and without considering cloud multiple scattering and terrain factors on different timescales in terms of accuracy.

		Case1	Case2	Case3	Case4
Instantaneous timescale	RMSE ($W m^{-2}$)	192.90	177.77	174.52	158.19
	MB ($W m^{-2}$)	57.23	12.04	51.58	6.13
	MAE ($W m^{-2}$)	132.48	119.71	121.74	109.36
	R	0.69	0.65	0.73	0.70
Ten-day timescale	RMSE ($W m^{-2}$)	96.54	80.79	87.53	73.45
	MB ($W m^{-2}$)	56.79	11.39	51.17	5.63
	MAE ($W m^{-2}$)	77.52	63.42	70.98	59.28
	R	0.87	0.81	0.89	0.83
Monthly timescale	RMSE ($W m^{-2}$)	84.50	66.45	77.44	62.03



MB (W m^{-2})	57.58	11.99	51.61	6.02
MAE (W m^{-2})	69.78	53.04	63.80	50.59
R	0.90	0.83	0.91	0.85

415

As shown in Table 5, the RMSE of case 1 reaches nearly 200 W m^{-2} at the instantaneous scale, nearly 100 W m^{-2} at the ten-day scale, and more than 80 W m^{-2} at the monthly scale, all of which are the highest among the four cases. As mentioned earlier, the estimated DSR of the SETORS station is more vulnerable to clouds. The RMSE of the SETORS station is reduced by 15%-19% when cloud multiple scattering is considered. Hence, ignoring the multiple scattering of clouds may lead to large errors in the case of high cloud cover. The verification results are improved when multiple cloud scattering and varying topography are introduced, and the RMSE is reduced by 8%-25%. Obviously, Case 4 shows the lowest RMSE, MB, MAE, and comparable R values compared with the other three cases. This reflects that when estimating DSR under all-sky conditions over the TP, the effects of terrain and cloud multiscattering cannot be simply ignored.

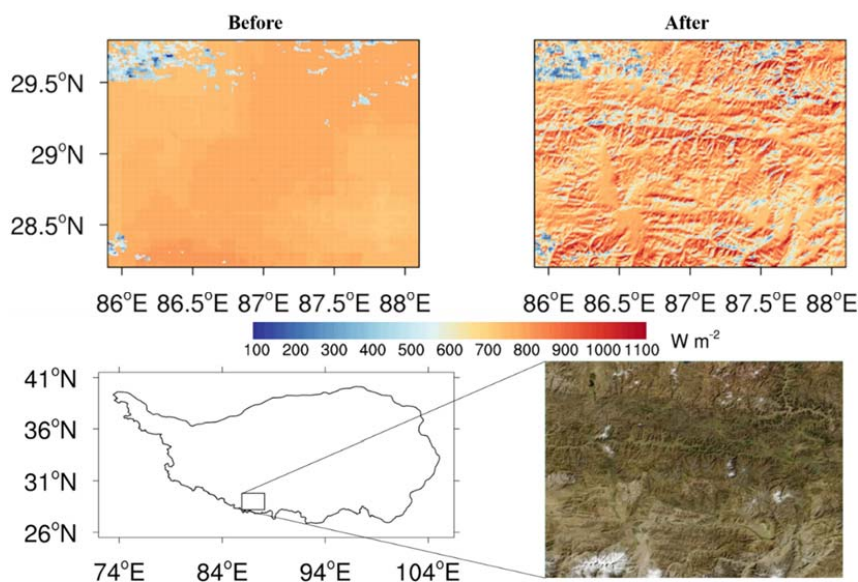


Figure 7. DSR estimated before terrain correction (left) and after terrain correction (right) over the TP at 10:30 LT on 10 January 2008.

To show the impact of varying topography on DSR, the spatial DSR pattern in a subarea of the TP before and after terrain correction is shown under relatively clear-sky conditions (Fig. 7). Before terrain

430



correction, the value of DSR is uniform, and the spatial texture is relatively smooth. The majority of the selected areas show relatively fixed values ($\sim 750 \text{ W m}^{-2}$), except for the parts covered by clouds, which show obviously low values. In contrast, the DSR values show high spatial dynamics, and it is easy to identify some subtle changes. The spatial gradient of DSR on the sunny and shady slope hillsides is obvious, and the higher parts receive more solar radiation. This is consistent with the surface features shown by the satellite images in the lower right corner.

5 Summary

Various satellite-based methods for estimating DSR have been developed during the past few decades, but some of them rarely operate effectively over the TP due to its complex terrain, high elevation, and unique climatology. Current surface radiation products ignore the influence of topographic variability on the DSR by simply assuming that the surface is horizontal and uniform, resulting in unreliable estimations in rugged regions. Due to the complexity and heterogeneity of the underlying surface of the TP, it is indispensable to consider the topographic variability in the process of DSR estimation. However, few models take the terrain effect into account on the large spatial scale of the whole TP. Unlike aerosol scattering and Rayleigh scattering, multiple scattering plays an important role in DSR attenuations caused by clouds. However, radiative extinctions due to cloud multiscattering tend to be ignored in existing DSR estimation methods under cloudy-sky conditions.

Thus, an improved parameterization scheme for deriving DSR over the TP under all-sky conditions is proposed in this paper. Based on meteorological forcing data and satellite data, the effects caused by ozone, aerosol, water vapor, Rayleigh scattering, permanent gas, cloud single scattering, cloud multiple scattering and topography are comprehensively considered in the improved parameterization scheme. The estimated DSR was validated against in situ observations collected at 12 stations over the TP, which cover a variety of elevations, climates, and land cover types. The validation results on different temporal scales show that the derived DSR based on the developed scheme is in good agreement with ground measurements. By comparing with existing widely used DSR products based on the same in situ observations, the derived DSR of this study performed better with the smallest RMSE, the lowest absolute value MB and the comparable R values on different spatiotemporal scales. Furthermore, the derived DSR of this study can capture the temporal variation characteristics as revealed by in situ



observations. The proposed methodology also provided reasonable spatial distribution patterns.
460 Specifically, this method demonstrated its superiority in characterizing more details and high dynamics
of the spatial pattern of DSR due to its higher resolution (1 km) and terrain correction. In addition, the
differences in the verification results and spatial distribution of different DSR products also prove that
there are still great uncertainties in current DSR products over the TP.

It should be noted that there are still some discrepancies for estimated DSR. Several reasons may
465 contribute to these discrepancies. First, the accuracy of the parameterization method depends on the
accuracy of the input data to some extent, such as cloud and aerosol information. At present, the
inhomogeneity of the horizontal and vertical directions of clouds in nature cannot be fully reflected from
the plan-parallel assumption, which is used for most cloud physical parameter inversions (Letu et al.,
2020). The defects will lead to uncertainties in cloud parameters. For the input atmospheric parameters,
470 the retrieval of AOD is quite challenging. The current popular “dark target” algorithm cannot deal well
with AOD retrievals on bright surfaces, such as snow/ice cover. Some studies have shown that MODIS
AOD products have high uncertainties in the TP compared with other regions (Wang et al., 2007; Xu et
al., 2015). Second, there are many snow/ice covers in the TP, while snow/ice and clouds are hard to
distinguish due to their similar reflective optical characteristics in many spectral regions. The ground
475 radiation field becomes extremely complex when the surface is covered by snow/ice. These factors make
it still a very challenging task to estimate the DSR on snow/ice cover thus far, especially under cloudy-
sky conditions. Finally, kilometer-level satellite-based DSR is susceptible to the 3D radiative effects of
clouds. It is difficult to tackle the 3D variability of clouds in DSR retrieval algorithms, especially for
instantaneous DSR (Huang et al., 2019). Furthermore, because convective clouds are abundant and easily
480 lead to precipitation over the TP (Fu et al., 2020), the 3D effect of clouds may be more difficult to address
on the TP.

The improved parameterization scheme can provide an independent reference for surface radiation
budget and land–atmosphere interaction studies over the TP. New-generation geostationary satellites with
higher temporal and spectral resolutions, such as FengYun-4 and Himawari-8, have been launched
485 successfully (Bessho et al., 2016; Guo et al., 2017). This allows us to further expand this method in the
future to obtain more details of surface radiation components over the TP.



Appendix A

$$\tau_{b,ctr} = \max(0, \tau_a \tau_{oz} \tau_g \tau_w - 0.013) \cos \theta, \quad (\text{A1})$$

$$\tau_{d,ctr} = \max(0, \tau_{oz} \tau_g \tau_w (1 - \tau_r \tau_a) + 0.013) \frac{(\cos s)^2}{2 \sin \alpha}, \quad (\text{A2})$$

$$490 \quad \tau_{r,ctr} = \rho_g (0.271 + 0.706 \max(0, \tau_a \tau_{oz} \tau_g \tau_w - 0.013)) \frac{(\sin s)^2}{2 \sin \alpha}, \quad (\text{A3})$$

where τ_a , τ_{oz} , τ_g , τ_w and τ_r refer to the broadband radiative transmittance for ozone aerosol extinction (aerosol scattering and absorption), ozone absorption, permanent gas absorption, water vapor absorption, and Rayleigh scattering, respectively. The above transmittances, τ_a , τ_{oz} , τ_g , τ_w , and τ_r , were obtained primarily by the parameterizations of Yang et al. (2006a).

$$495 \quad \tau_{b,cl,d} = \tau_{oz} \tau_w \tau_g \tau_r \tau_a \tau_{cl,d} \cos \theta, \quad (\text{A4})$$

$$\tau_{d,cl,d} = (\tau_{d,cl,d}^{r,ms} + \tau_{d,cl,d}^{a,ms} + \tau_{d,cl,d}^{ss,ms}) \frac{(\cos s)^2}{2 \sin \alpha}, \quad (\text{A5})$$

$$\tau_{d,cl,d}^{r,ms} = 0.5 \tau_{oz} \tau_w \tau_g \tau_{aa} (1 - \tau_r) \tau_{cl,d,a} \tau_{cl,d,ms}, \quad (\text{A6})$$

$$\tau_{d,cl,d}^{a,ms} = f_{aer}(\mu) \tau_{oz} \tau_w \tau_g \tau_{aa} \tau_r (1 - \tau_{as}) \tau_{cl,d,a} \tau_{cl,d,ms}, \quad (\text{A7})$$

$$\tau_{d,cl,d}^{ss,ms} = \tau_{oz} \tau_w \tau_g \tau_a \tau_r \tau_{cl,d,a} (1 - \tau_{cl,d,ss}) \tau_{cl,d,ms}, \quad (\text{A8})$$

$$500 \quad \tau_{r,cl,d} = \rho_g (0.271 + 0.706 \tau_{oz} \tau_w \tau_g \tau_r \tau_a \tau_{cl,d}) \frac{(\sin s)^2}{2 \sin \alpha}, \quad (\text{A9})$$

where $\tau_{cl,d}$, $\tau_{cl,d,a}$ and $\tau_{cl,d,ss}$ refer to the broadband radiative transmittance, broadband radiative absorption transmittance and broadband radiative scattering transmittance caused by cloud single-scattering actions, respectively. τ_{aa} , τ_{as} and $\tau_{cl,d,ms}$ refer to the broadband radiative transmittance for aerosol absorption, aerosol scattering and cloud radiation multiple actions, respectively.

505 μ is the cosine of the solar zenith angle, and $f_{aer}(\mu)$ is the aerosol forward scattering fraction, which is parameterized as

$$f_{aer}(\mu) = 0.364 + 0.632\mu - 0.245\mu^2, \quad (\text{A10})$$

$\tau_{cl,d}$, $\tau_{cl,d,a}$, $\tau_{cl,d,ss}$, $\tau_{cl,d,ms}$, τ_{aa} and τ_{as} can be described as follows:

$$\tau_{cl,d} = \exp(-aCWP/\mu CER), \quad (\text{A11})$$

$$510 \quad \tau_{cl,d,a} = \exp(-bCWP/\mu CER), \quad (\text{A12})$$



$$\tau_{cld,ss} = \exp(-c_1 \mu CWP^{c_2} / (\mu^{c_2} + c_3 CWP^{c_2})), \quad (A13)$$

$$\tau_{cld,ms} = \exp\left(\frac{-CWP/CER}{d_1 + d_2 CWP/CER + d_3 \sqrt{CWP/CER}}\right), \quad (A14)$$

$$\tau_{aa} = \tau_a^{(1-\omega_a)}, \quad (A15)$$

$$\tau_{as} = \tau_a^{\omega_a}, \quad (A16)$$

515 The atmosphere hemispherical albedo $\rho_{a,cld}$ is parameterized as:

$$\rho_{a,cld} = 0.086 + \frac{CWP/CER}{e_1 + e_2 CWP/CER + e_3 \sqrt{CWP/CER}} \quad (A17)$$

where the coefficients ($a, b, c_1, c_2, c_3, d_1, d_2, d_3, e_1, e_2, e_3$) for different types of clouds can be found in the study by Huang et al. (2018). ω_a is the aerosol single-scattering albedo, and its value depends on the type of aerosol (Levy et al., 2007; Huang et al., 2020).

520 Here, we assume that ozone absorption and air molecule scattering both take place above clouds (Qin et al., 2015; Tang et al., 2016; Huang et al., 2018). $\tau_{d,cld}^{r,ms}$ and $\tau_{d,cld}^{a,ms}$ can represent the part of diffuse radiation (caused by Rayleigh scattering and aerosol scattering, respectively) that finally reaches the surface after cloud multiscattering. $\tau_{d,cld}^{ss,ms}$ can represent the part of diffuse radiation (caused by cloud single scattering) that finally reaches the surface after cloud multiscattering.

525 The topographic effects are taken into account in DSR estimation parameterization schemes by the solar zenith angle θ , the solar altitude angle α and the tilt angle of the surface (slope) s . According to this knowledge, Chen et al. (2013) provided a scheme that can be applied in mountainous areas based on high-resolution DEM datasets.

$$\sin \alpha = \sin L \sin \delta_s + \cos L \cos \delta_s \cos h_s, \quad (A18)$$

$$\begin{aligned} 530 \quad \cos \theta &= \sin L \sin \delta_s \cos s - \cos L \sin \delta_s \sin s \cos \gamma \\ &+ \cos L \cos \delta_s \cos s \cos h_s + \sin L \cos \delta_s \sin s \cos \gamma \cos h_s \\ &+ \sin L \cos \delta_s \sin s \sin h_s, \end{aligned} \quad (A19)$$

where L is latitude. δ_s is the declination of the earth. h_s is the hour angle. γ is the surface aspect angle.

535 The BSA and WSA are the surface albedos under the condition of complete direct and diffuse solar radiation, not the actual surface albedo. According to Pinty et al. (2005) and Stokes and Schwartz (1994),



the actual surface albedo can be obtained by

$$r = 0.122 + 0.85 \exp(-4.8\mu), \quad (\text{A20})$$

$$\rho_g = rBSA + (1 - r)WSA, \quad (\text{A21})$$

540 **Data availability**

The in situ measurements used in this study were obtained from the National Tibetan Plateau Data Center (<http://data.tpdc.ac.cn>) and National Cryosphere Desert Data Center (<http://www.ncdc.ac.cn>). The MODIS products we used can be freely downloaded via the NASA website (<https://modis.gsfc.nasa.gov/>).

Author contributions.

545 PL and ZL designed and implemented the study. PL prepared the manuscript with help from ZL, YM and YF. MC and XW contributed to analysis of the data. YQ and ZW collected the in situ data. All commented on the paper.

Acknowledgments

This work was funded by National Natural Science Foundation of China (Grant No. 41875031); the
550 Second Tibetan Plateau Scientific Expedition and Research (STEP) Program (Grant No. 2019QZKK0103); The Chinese Academy of Sciences (Grant No. XDA20060101); National Natural Science Foundation of China (Grant No. 91837208, 41522501, 41275028) and CLIMATE-Pan-TPE in the framework of the ESA-MOST Dragon 5 Programme (Grant ID 58516).

Competing interests.

555 The authors declare that they have no conflict of interest.

Reference

Ahn, C., Torres, O., and Bhartia, P. K.: Comparison of Ozone Monitoring Instrument UV Aerosol Products with Aqua/Moderate Resolution Imaging Spectroradiometer and Multiangle Imaging Spectroradiometer observations in 2006, *Journal of Geophysical Research*, 113,



- 560 10.1029/2007jd008832, 2008.
- Bessho, K., Date, K., Hayashi, M., Ikeda, A., Imai, T., Inoue, H., Kumagai, Y., Miyakawa, T., Murata, H., Ohno, T., Okuyama, A., Oyama, R., Sasaki, Y., Shimazu, Y., Shimoji, K., Sumida, Y., Suzuki, M., Taniguchi, H., Tsuchiyama, H., Uesawa, D., Yokota, H., and Yoshida, R.: An Introduction to Himawari-8/9— Japan’s New-Generation Geostationary Meteorological Satellites, 565 Journal of the Meteorological Society of Japan. Ser. II, 94, 151-183, 10.2151/jmsj.2016-009, 2016.
- Bisht, G. and Bras, R. L.: Estimation of net radiation from the MODIS data under all sky conditions: Southern Great Plains case study, Remote Sensing of Environment, 114, 1522-1534, 10.1016/j.rse.2010.02.007, 2010.
- Bisht, G., Venturini, V., Islam, S., and Jiang, L.: Estimation of the net radiation using MODIS (Moderate 570 Resolution Imaging Spectroradiometer) data for clear sky days, Remote Sensing of Environment, 97, 52-67, 10.1016/j.rse.2005.03.014, 2005.
- Chen, J., Hu, Z., Dou, S., and Zeyu, Q.: Yin–Yang Slope problem along Qinghai–Tibetan Lines and its radiation mechanism, Cold Regions Science and Technology, 44, 217-224, 10.1016/j.coldregions.2005.12.001, 2006.
- 575 Chen, X., Su, Z., Ma, Y., Yang, K., and Wang, B.: Estimation of surface energy fluxes under complex terrain of Mt. Qomolangma over the Tibetan Plateau, Hydrology and Earth System Sciences, 17, 1607-1618, 10.5194/hess-17-1607-2013, 2013.
- Decker, M., Brunke, M. A., Wang, Z., Sakaguchi, K., Zeng, X., and Bosilovich, M. G.: Evaluation of the Reanalysis Products from GSFC, NCEP, and ECMWF Using Flux Tower Observations, Journal of 580 Climate, 25, 1916-1944, 10.1175/jcli-d-11-00004.1, 2012.
- Fu, Y., Ma, Y., Zhong, L., Yang, Y., Guo, X., Wang, C., Xu, X., Yang, K., Xu, X., Liu, L., Fan, G., Li, Y., and Wang, D.: Land-surface processes and summer-cloud-precipitation characteristics in the Tibetan Plateau and their effects on downstream weather: a review and perspective, Natl Sci Rev, 7, 500-515, 10.1093/nsr/nwz226, 2020.
- 585 Fujinami, H., Nomura, S., and Yasunari, T.: Characteristics of Diurnal Variations in Convection and Precipitation over the Southern Tibetan Plateau during Summer, Sola, 1, 49-52, 10.2151/sola.2005-014, 2005.
- Gueymard, C. A.: Clear-sky irradiance predictions for solar resource mapping and large-scale



- 590 applications: Improved validation methodology and detailed performance analysis of 18 broadband radiative models, *Solar Energy*, 86, 2145-2169, 10.1016/j.solener.2011.11.011, 2012.
- Guo, Q., Lu, F., Wei, C., Zhang, Z., and Yang, J.: Introducing the New Generation of Chinese Geostationary Weather Satellites, Fengyun-4, *Bulletin of the American Meteorological Society*, 98, 1637-1658, 10.1175/bams-d-16-0065.1, 2017.
- Hakuba, M. Z., Folini, D., Sanchez-Lorenzo, A., and Wild, M.: Spatial representativeness of ground-based solar radiation measurements, *Journal of Geophysical Research: Atmospheres*, 118, 8585-8597, 10.1002/jgrd.50673, 2013.
- 595 Hans, H., Bell, W., Berrisford, P., Andras, H., Muñoz-Sabater, J., Nicolas, J., Raluca, R., Dinand, S., Adrian, S., Cornel, S., and Dick, D.: Global reanalysis: goodbye ERA-Interim, hello ERA5, 2019.
- He, J., Yang, K., Tang, W., Lu, H., Qin, J., Chen, Y., and Li, X.: The first high-resolution meteorological forcing dataset for land process studies over China, *Sci Data*, 7, 25, 10.1038/s41597-020-0369-y, 600 2020.
- Hong, S.-Y., Kanamitsu, M., Kim, J.-E., and Koo, M.-S.: Effects of Diurnal Cycle on a Simulated Asian Summer Monsoon, *Journal of Climate*, 25, 8394-8408, 10.1175/jcli-d-12-00069.1, 2012.
- Huang, C., Shi, H., Gao, L., Liu, M., Chen, Q., Fu, D., Wang, S., Yuan, Y., and Xia, X. a.: Fengyun-4 605 Geostationary Satellite-Based Solar Energy Nowcasting System and Its Application in North China, *Adv Atmos Sci*, 39, 1316-1328, 10.1007/s00376-022-1464-0, 2022.
- Huang, G., Li, X., Lu, N., Wang, X., and He, T.: A General Parameterization Scheme for the Estimation of Incident Photosynthetically Active Radiation Under Cloudy Skies, *IEEE Transactions on Geoscience and Remote Sensing*, 58, 6255-6265, 10.1109/tgrs.2020.2976103, 2020.
- 610 Huang, G., Li, X., Ma, M., Li, H., and Huang, C.: High resolution surface radiation products for studies of regional energy, hydrologic and ecological processes over Heihe river basin, northwest China, *Agric. For. Meteorol.*, 230-231, 67-78, 10.1016/j.agrformet.2016.04.007, 2016a.
- Huang, G., Liang, S., Lu, N., Ma, M., and Wang, D.: Toward a Broadband Parameterization Scheme for Estimating Surface Solar Irradiance: Development and Preliminary Results on MODIS Products, 615 *Journal of Geophysical Research: Atmospheres*, 123, 1180-112, 193, 10.1029/2018jd028905, 2018.
- Huang, G., Li, X., Huang, C., Liu, S., Ma, Y., and Chen, H.: Representativeness errors of point-scale ground-based solar radiation measurements in the validation of remote sensing products, *Remote*



- Sensing of Environment, 181, 198-206, 10.1016/j.rse.2016.04.001, 2016b.
- Huang, G., Li, Z., Li, X., Liang, S., Yang, K., Wang, D., and Zhang, Y.: Estimating surface solar irradiance
620 from satellites: Past, present, and future perspectives, Remote Sensing of Environment, 233,
10.1016/j.rse.2019.111371, 2019.
- Hwang, K., Choi, M., Lee, S. O., and Seo, J.-W.: Estimation of instantaneous and daily net radiation from
MODIS data under clear sky conditions: a case study in East Asia, Irrigation Science, 31, 1173-
1184, 10.1007/s00271-012-0396-3, 2012.
- 625 Immerzeel, W. W., van Beek, L. P., and Bierkens, M. F.: Climate change will affect the Asian water
towers, Science, 328, 1382-1385, 10.1126/science.1183188, 2010.
- Kuang, X. and Jiao, J. J.: Review on climate change on the Tibetan Plateau during the last half century,
Journal of Geophysical Research: Atmospheres, 121, 3979-4007, 10.1002/2015jd024728, 2016.
- Kukulies, J., Chen, D., and Wang, M.: Temporal and spatial variations of convection, clouds and
630 precipitation over the Tibetan Plateau from recent satellite observations. Part II: Precipitation
climatology derived from global precipitation measurement mission, International Journal of
Climatology, 40, 4858-4875, 10.1002/joc.6493, 2020.
- Letu, H., Shi, J., Li, M., Wang, T., Shang, H., Lei, Y., Ji, D., Wen, J., Yang, K., and Chen, L.: A review of
the estimation of downward surface shortwave radiation based on satellite data: Methods, progress
635 and problems, Science China Earth Sciences, 63, 774-789, 10.1007/s11430-019-9589-0, 2020.
- Levy, R. C., Remer, L. A., and Dubovik, O.: Global aerosol optical properties and application to Moderate
Resolution Imaging Spectroradiometer aerosol retrieval over land, Journal of Geophysical Research:
Atmospheres, 112, 10.1029/2006jd007815, 2007.
- Li, J., Tang, W., Yang, K., Xie, Y., Gueymard, C. A., Qin, J., and Sengupta, M.: An Improved Algorithm
640 for Estimating Surface Shortwave Radiation: Preliminary Evaluation With MODIS Products, IEEE
Transactions on Geoscience and Remote Sensing, 60, 1-9, 10.1109/tgrs.2021.3098742, 2022.
- Li, Y., Wang, Y., Song, Y., Hu, L., Gao, S., and Rong, F.: Characteristics of Summer Convective Systems
Initiated over the Tibetan Plateau. Part I: Origin, Track, Development, and Precipitation, Journal of
Applied Meteorology and Climatology, 47, 2679-2695, 10.1175/2008jamc1695.1, 2008.
- 645 Li, Z., Lyu, S., Wen, L., Zhao, L., Ao, Y., and Meng, X.: Study of freeze-thaw cycle and key radiation
transfer parameters in a Tibetan Plateau lake using LAKE2.0 model and field observations, Journal



- of *Glaciology*, 67, 91-106, 10.1017/jog.2020.87, 2020.
- Li, Z., Lyu, S., Wen, L., Zhao, L., Ao, Y., and Wang, S.: Effect of a cold, dry air incursion on atmospheric boundary layer processes over a high-altitude lake in the Tibetan Plateau, *Atmospheric Research*, 650 185, 32-43, 10.1016/j.atmosres.2016.10.024, 2017.
- Li, Z., Lyu, S., Chen, S., Ao, Y., Zhao, L., Chen, H., and Meng, X.: Observed characteristics of the water and heat transfer of the soil–snow–atmosphere system through the snowpack in the eastern Tibetan Plateau, *Atmospheric Research*, 248, 10.1016/j.atmosres.2020.105195, 2021.
- Li, Z. Q., Barker, H. W., and Moreau, L.: The Variable Effect of Clouds on Atmospheric Absorption of 655 Solar-Radiation, *Nature*, 376, 486-490, DOI 10.1038/376486a0, 1995.
- Li, Z. Q., Moreau, L., and Arking, A.: On solar energy disposition: A perspective from observation and modeling, *Bulletin of the American Meteorological Society*, 78, 53-70, Doi 10.1175/1520-0477(1997)078<0053:Osedap>2.0.Co;2, 1997.
- Liang, S., Wang, D., He, T., and Yu, Y.: Remote sensing of earth's energy budget: synthesis and review, 660 *International Journal of Digital Earth*, 12, 737-780, 10.1080/17538947.2019.1597189, 2019.
- Liang, S., Wang, K., Zhang, X., and Wild, M.: Review on Estimation of Land Surface Radiation and Energy Budgets From Ground Measurement, Remote Sensing and Model Simulations, *IEEE Journal of Selected Topics in Applied Earth Observations and Remote Sensing*, 3, 225-240, 10.1109/jstars.2010.2048556, 2010.
- 665 Liang, S., Zheng, T., Liu, R., Fang, H., Tsay, S.-C., and Running, S.: Estimation of incident photosynthetically active radiation from Moderate Resolution Imaging Spectrometer data, *Journal of Geophysical Research*, 111, 10.1029/2005jd006730, 2006.
- Loeb, N. G., Kato, S., Rose, F. G., Doelling, D. R., Rutan, D. A., Caldwell, T. E., Yu, L., and Weller, R. A.: Surface Irradiances Consistent with CERES-Derived Top-of-Atmosphere Shortwave and 670 Longwave Irradiances, *Journal of Climate*, 26, 2719-2740, 10.1175/jcli-d-12-00436.1, 2013.
- Lu, N., Liu, R., Liu, J., and Liang, S.: An algorithm for estimating downward shortwave radiation from GMS 5 visible imagery and its evaluation over China, *Journal of Geophysical Research*, 115, 10.1029/2009jd013457, 2010.
- Lu, N., Qin, J., Yang, K., and Sun, J.: A simple and efficient algorithm to estimate daily global solar 675 radiation from geostationary satellite data, *Energy*, 36, 3179-3188, 10.1016/j.energy.2011.03.007,



- 2011.
- Ma, R., Letu, H., Yang, K., Wang, T., Shi, C., Xu, J., Shi, J., Shi, C., and Chen, L.: Estimation of Surface Shortwave Radiation From Himawari-8 Satellite Data Based on a Combination of Radiative Transfer and Deep Neural Network, *IEEE Transactions on Geoscience and Remote Sensing*, 58, 680 5304-5316, 10.1109/tgrs.2019.2963262, 2020a.
- Ma, Y., Ma, W., Zhong, L., Hu, Z., Li, M., Zhu, Z., Han, C., Wang, B., and Liu, X.: Monitoring and Modeling the Tibetan Plateau's climate system and its impact on East Asia, *Sci Rep*, 7, 44574, 10.1038/srep44574, 2017.
- Ma, Y., Zhu, Z., Zhong, L., Wang, B., Han, C., Wang, Z., Wang, Y., Lu, L., Amatya, P. M., Ma, W., and 685 Hu, Z.: Combining MODIS, AVHRR and in situ data for evapotranspiration estimation over heterogeneous landscape of the Tibetan Plateau, *Atmospheric Chemistry and Physics*, 14, 1507-1515, 10.5194/acp-14-1507-2014, 2014.
- Ma, Y., Wang, Y., Wu, R., Hu, Z., Yang, K., Li, M., Ma, W., Zhong, L., Sun, F., Chen, X., Zhu, Z., Wang, S., and Ishikawa, H.: Recent advances on the study of atmosphere-land interaction observations on 690 the Tibetan Plateau, *Hydrology and Earth System Sciences*, 13, 1103-1111, DOI 10.5194/hess-13-1103-2009, 2009.
- Ma, Y., Hu, Z., Xie, Z., Ma, W., Wang, B., Chen, X., Li, M., Zhong, L., Sun, F., Gu, L., Han, C., Zhang, L., Liu, X., Ding, Z., Sun, G., Wang, S., Wang, Y., and Wang, Z.: A long-term (2005–2016) dataset of hourly integrated land–atmosphere interaction observations on the Tibetan Plateau, *Earth System 695 Science Data*, 12, 2937-2957, 10.5194/essd-12-2937-2020, 2020b.
- Ma, Y. M., Kang, S. C., Zhu, L. P., Xu, B. Q., Tian, L. D., and Yao, T. D.: TIBETAN OBSERVATION AND RESEARCH PLATFORM Atmosphere-Land Interaction over a Heterogeneous Landscape, *Bulletin of the American Meteorological Society*, 89, 1487+, 10.1175/2008bams2545.1, 2008.
- Masuda, K., Leighton, H. G., and Li, Z. Q.: A New Parameterization for the Determination of Solar Flux 700 Absorbed at the Surface from Satellite Measurements, *Journal of Climate*, 8, 1615-1629, Doi 10.1175/1520-0442(1995)008<1615:Anpftd>2.0.Co;2, 1995.
- Niemela, S., Raisanen, P., and Savijarvi, H.: Comparison of surface radiative flux parameterizations - Part II. Shortwave radiation, *ATMOSPHERIC RESEARCH*, 58, 141-154, 10.1016/S0169-8095(01)00085-0, 2001.



- 705 Olson, M. and Rupper, S.: Impacts of topographic shading on direct solar radiation for valley glaciers in complex topography, *The Cryosphere*, 13, 29-40, 10.5194/tc-13-29-2019, 2019.
- Piao, S., Ciais, P., Huang, Y., Shen, Z., Peng, S., Li, J., Zhou, L., Liu, H., Ma, Y., Ding, Y., Friedlingstein, P., Liu, C., Tan, K., Yu, Y., Zhang, T., and Fang, J.: The impacts of climate change on water resources and agriculture in China, *Nature*, 467, 43-51, 10.1038/nature09364, 2010.
- 710 Pinker, R. T. and Laszlo, I.: Modeling Surface Solar Irradiance for Satellite Applications on a Global Scale, *J Appl Meteorol*, 31, 194-211, Doi 10.1175/1520-0450(1992)031<0194:Mssifs>2.0.Co;2, 1992.
- Pinker, R. T., Zhang, B., and Dutton, E. G.: Do satellites detect trends in surface solar radiation?, *SCIENCE*, 308, 850-854, 10.1126/science.1103159, 2005.
- 715 Pinker, R. T., Li, X., Meng, W., and Yegorova, E. A.: Toward improved satellite estimates of short-wave radiative fluxes—Focus on cloud detection over snow: 2. Results, *Journal of Geophysical Research*, 112, 10.1029/2005jd006699, 2007.
- Pinty, B., Lattanzio, A., Martonchik, J. V., Verstraete, M. M., Gobron, N., Taberner, M., Widlowski, J. L., Dickinson, R. E., and Govaerts, Y.: Coupling diffuse sky radiation and surface albedo, *Journal of the Atmospheric Sciences*, 62, 2580-2591, Doi 10.1175/Jas3479.1, 2005.
- 720 Platnick, S., King, M. D., Ackerman, S. A., Menzel, W. P., Baum, B. A., Riedi, J. C., and Frey, R. A.: The MODIS cloud products: algorithms and examples from terra, *IEEE Transactions on Geoscience and Remote Sensing*, 41, 459-473, 10.1109/tgrs.2002.808301, 2003.
- Platnick, S., Meyer, K. G., King, M. D., Wind, G., Amarasinghe, N., Marchant, B., Arnold, G. T., Zhang, 725 Z., Hubanks, P. A., Holz, R. E., Yang, P., Ridgway, W. L., and Riedi, J.: The MODIS cloud optical and microphysical products: Collection 6 updates and examples from Terra and Aqua, *IEEE Trans Geosci Remote Sens*, 55, 502-525, 10.1109/TGRS.2016.2610522, 2017.
- Qin, J., Chen, Z., Yang, K., Liang, S., and Tang, W.: Estimation of monthly-mean daily global solar radiation based on MODIS and TRMM products, *Applied Energy*, 88, 2480-2489, 730 10.1016/j.apenergy.2011.01.018, 2011.
- Qin, J., Tang, W., Yang, K., Lu, N., Niu, X., and Liang, S.: An efficient physically based parameterization to derive surface solar irradiance based on satellite atmospheric products, *Journal of Geophysical Research: Atmospheres*, 120, 4975-4988, 10.1002/2015jd023097, 2015.



- Qiu, J.: The third pole, *NATURE*, 454, 393-396, 10.1038/454393a, 2008.
- 735 Roupioz, L., Jia, L., Nerry, F., and Menenti, M.: Estimation of Daily Solar Radiation Budget at Kilometer Resolution over the Tibetan Plateau by Integrating MODIS Data Products and a DEM, *Remote Sensing*, 8, 10.3390/rs8060504, 2016.
- Schaaf, C. B., Gao, F., Strahler, A. H., Lucht, W., Li, X. W., Tsang, T., Strugnell, N. C., Zhang, X. Y., Jin, Y. F., Muller, J. P., Lewis, P., Barnsley, M., Hobson, P., Disney, M., Roberts, G., Dunderdale, M.,
740 Doll, C., d'Entremont, R. P., Hu, B. X., Liang, S. L., Privette, J. L., and Roy, D.: First operational BRDF, albedo nadir reflectance products from MODIS, *REMOTE SENSING OF ENVIRONMENT*, 83, 135-148, 10.1016/S0034-4257(02)00091-3, 2002.
- Sengupta, M., Xie, Y., Lopez, A., Habte, A., Maclaurin, G., and Shelby, J.: The National Solar Radiation Data Base (NSRDB), *Renewable and Sustainable Energy Reviews*, 89, 51-60,
745 10.1016/j.rser.2018.03.003, 2018.
- Stephens, G. L., Li, J., Wild, M., Clayton, C. A., Loeb, N., Kato, S., L'Ecuyer, T., Stackhouse, P. W., Lebsock, M., and Andrews, T.: An update on Earth's energy balance in light of the latest global observations, *Nature Geoscience*, 5, 691-696, 10.1038/ngeo1580, 2012.
- Stokes, G. M. and Schwartz, S. E.: The Atmospheric Radiation - Measurement (Arm) Program -
750 Programmatic Background and Design of the Cloud and Radiation Test-Bed, *Bulletin of the American Meteorological Society*, 75, 1201-1221, Doi 10.1175/1520-0477(1994)075<1201:Tarmpp>2.0.Co;2, 1994.
- Tanaka, K., Ishikawa, H., Hayashi, T., Tamagawa, I., and Ma, Y. M.: Surface energy budget at Amdo on the Tibetan Plateau using GAME/Tibet IOP98 data, *J Meteorol Soc Jpn*, 79, 505-517, DOI
755 10.2151/jmsj.79.505, 2001.
- Tang, W., Yang, K., Qin, J., Li, X., and Niu, X.: A 16-year dataset (2000–2015) of high-resolution (3 h, 10 km) global surface solar radiation, *Earth System Science Data*, 11, 1905-1915, 10.5194/essd-11-1905-2019, 2019.
- Tang, W., Qin, J., Yang, K., Liu, S., Lu, N., and Niu, X.: Retrieving high-resolution surface solar radiation
760 with cloud parameters derived by combining MODIS and MTSAT data, *Atmospheric Chemistry and Physics*, 16, 2543-2557, 10.5194/acp-16-2543-2016, 2016.
- Tovar, J., Olmo, F. J., and Aladosarboledas, L.: LOCAL-SCALE VARIABILITY OF SOLAR-



- RADIATION IN A MOUNTAINOUS REGION, *J Appl Meteorol*, 34, 2316-2322, 10.1175/1520-0450(1995)034<2316:LSVOSR>2.0.CO;2, 1995.
- 765 Wang, G., Wang, T., and Xue, H.: Validation and comparison of surface shortwave and longwave radiation products over the three poles, *International Journal of Applied Earth Observation and Geoinformation*, 104, 10.1016/j.jag.2021.102538, 2021.
- Wang, K. and Dickinson, R. E.: Contribution of solar radiation to decadal temperature variability over land, *Proc Natl Acad Sci U S A*, 110, 14877-14882, 10.1073/pnas.1311433110, 2013.
- 770 Wang, L., Gong, W., Hu, B., Lin, A., Li, H., and Zou, L.: Modeling and analysis of the spatiotemporal variations of photosynthetically active radiation in China during 1961–2012, *Renewable and Sustainable Energy Reviews*, 49, 1019-1032, 10.1016/j.rser.2015.04.174, 2015.
- Wang, L., Xin, J., Wang, Y., Li, Z., Liu, G., and Li, J.: Evaluation of the MODIS aerosol optical depth retrieval over different ecosystems in China during EAST-AIRE, *Atmospheric Environment*, 41, 775 7138-7149, 10.1016/j.atmosenv.2007.05.001, 2007.
- Wei, Y., Zhang, X., Hou, N., Zhang, W., Jia, K., and Yao, Y.: Estimation of surface downward shortwave radiation over China from AVHRR data based on four machine learning methods, *Solar Energy*, 177, 32-46, 10.1016/j.solener.2018.11.008, 2019.
- Wu, G., Liu, Y., He, B., Bao, Q., Duan, A., and Jin, F. F.: Thermal controls on the Asian summer monsoon, 780 *Sci Rep*, 2, 404, 10.1038/srep00404, 2012.
- Xie, Y., Sengupta, M., and Dudhia, J.: A Fast All-sky Radiation Model for Solar applications (FARMS): Algorithm and performance evaluation, *Solar Energy*, 135, 435-445, 10.1016/j.solener.2016.06.003, 2016.
- Xu, C., Ma, Y. M., You, C., and Zhu, Z. K.: The regional distribution characteristics of aerosol optical 785 depth over the Tibetan Plateau, *Atmospheric Chemistry and Physics*, 15, 12065-12078, 10.5194/acp-15-12065-2015, 2015.
- Xu, W., Ma, L., Ma, M., Zhang, H., and Yuan, W.: Spatial–Temporal Variability of Snow Cover and Depth in the Qinghai–Tibetan Plateau, *Journal of Climate*, 30, 1521-1533, 10.1175/jcli-d-15-0732.1, 2017.
- 790 Xu, X., Lu, C., Shi, X., and Gao, S.: World water tower: An atmospheric perspective, *Geophysical Research Letters*, 35, 10.1029/2008gl035867, 2008.



- Yang, D., Wang, W., and Xia, X. a.: A Concise Overview on Solar Resource Assessment and Forecasting, *Adv Atmos Sci*, 39, 1239-1251, 10.1007/s00376-021-1372-8, 2022.
- Yang, K., Koike, T., and Ye, B.: Improving estimation of hourly, daily, and monthly solar radiation by
795 importing global data sets, *Agric. For. Meteorol*, 137, 43-55, 10.1016/j.agrformet.2006.02.001,
2006a.
- Yang, K., He, J., Tang, W., Qin, J., and Cheng, C. C. K.: On downward shortwave and longwave
radiations over high altitude regions: Observation and modeling in the Tibetan Plateau, *Agric. For.
Meteorol*, 150, 38-46, 10.1016/j.agrformet.2009.08.004, 2010a.
- 800 Yang, K., Koike, T., Stackhouse, P., Mikovitz, C., and Cox, S. J.: An assessment of satellite surface
radiation products for highlands with Tibet instrumental data, *Geophysical Research Letters*, 33,
10.1029/2006gl027640, 2006b.
- Yang, K., Wu, H., Qin, J., Lin, C., Tang, W., and Chen, Y.: Recent climate changes over the Tibetan
Plateau and their impacts on energy and water cycle: A review, *Global and Planetary Change*, 112,
805 79-91, 10.1016/j.gloplacha.2013.12.001, 2014.
- Yang, K., Pinker, R. T., Ma, Y., Koike, T., Wonsick, M. M., Cox, S. J., Zhang, Y., and Stackhouse, P.:
Evaluation of satellite estimates of downward shortwave radiation over the Tibetan Plateau, *Journal
of Geophysical Research*, 113, 10.1029/2007jd009736, 2008.
- Yang, M., Nelson, F. E., Shiklomanov, N. I., Guo, D., and Wan, G.: Permafrost degradation and its
810 environmental effects on the Tibetan Plateau: A review of recent research, *Earth-Science Reviews*,
103, 31-44, 10.1016/j.earscirev.2010.07.002, 2010b.
- Yao, J., Zhao, L., Gu, L., Qiao, Y., and Jiao, K.: The surface energy budget in the permafrost region of
the Tibetan Plateau, *Atmospheric Research*, 102, 394-407, 10.1016/j.atmosres.2011.09.001, 2011.
- Yao, T., Thompson, L., Yang, W., Yu, W., Gao, Y., Guo, X., Yang, X., Duan, K., Zhao, H., Xu, B., Pu, J.,
815 Lu, A., Xiang, Y., Kattel, D. B., and Joswiak, D.: Different glacier status with atmospheric
circulations in Tibetan Plateau and surroundings, *Nature Climate Change*, 2, 663-667,
10.1038/nclimate1580, 2012.
- Zhang, H., Xin, X., Li, L., and Liu, Q.: Estimating global solar radiation using a hybrid parametric model
from MODIS data over the Tibetan Plateau, *Solar Energy*, 112, 373-382,
820 10.1016/j.solener.2014.12.015, 2015.



- Zhang, J., Zhao, L., Deng, S., Xu, W., and Zhang, Y.: A critical review of the models used to estimate solar radiation, *Renewable and Sustainable Energy Reviews*, 70, 314-329, 10.1016/j.rser.2016.11.124, 2017.
- Zhang, K., Zhao, L., Tang, W., Yang, K., and Wang, J.: Global and Regional Evaluation of the CERES Edition-4A Surface Solar Radiation and Its Uncertainty Quantification, *IEEE Journal of Selected Topics in Applied Earth Observations and Remote Sensing*, 15, 2971-2985, 10.1109/jstars.2022.3164471, 2022.
- 825
- Zhang, T., Stackhouse, P. W., Chandler, W. S., and Westberg, D. J.: Application of a global-to-beam irradiance model to the NASA GEWEX SRB dataset: An extension of the NASA Surface meteorology and Solar Energy datasets, *Solar Energy*, 110, 117-131, 10.1016/j.solener.2014.09.006, 830 2014.
- Zhao, C., Chen, Y., Li, J., Letu, H., Su, Y., Chen, T., and Wu, X.: Fifteen-year statistical analysis of cloud characteristics over China using Terra and Aqua Moderate Resolution Imaging Spectroradiometer observations, *International Journal of Climatology*, 39, 2612-2629, 10.1002/joc.5975, 2019a.
- 835
- Zhao, L., Zou, D., Hu, G., Wu, T., Du, E., Liu, G., Xiao, Y., Li, R., Pang, Q., Qiao, Y., Wu, X., Sun, Z., Xing, Z., Sheng, Y., Zhao, Y., Shi, J., Xie, C., Wang, L., Wang, C., and Cheng, G.: A synthesis dataset of permafrost thermal state for the Qinghai–Tibet (Xizang) Plateau, China, *Earth System Science Data*, 13, 4207-4218, 10.5194/essd-13-4207-2021, 2021.
- Zhao, P., Zhou, X., Chen, J., Liu, G., and Nan, S.: Global climate effects of summer Tibetan Plateau, 840 *Science Bulletin*, 64, 1-3, 10.1016/j.scib.2018.11.019, 2019b.
- Zhao, P., Xu, X., Chen, F., Guo, X., Zheng, X., Liu, L., Hong, Y., Li, Y., La, Z., Peng, H., Zhong, L., Ma, Y., Tang, S., Liu, Y., Liu, H., Li, Y., Zhang, Q., Hu, Z., Sun, J., Zhang, S., Dong, L., Zhang, H., Zhao, Y., Yan, X., Xiao, A., Wan, W., Liu, Y., Chen, J., Liu, G., Zhaxi, Y., and Zhou, X.: The Third Atmospheric Scientific Experiment for Understanding the Earth–Atmosphere Coupled System over 845 the Tibetan Plateau and Its Effects, *Bulletin of the American Meteorological Society*, 99, 757-776, 10.1175/bams-d-16-0050.1, 2018.
- Zhong, L., Ma, Y., Su, Z., and Salama, M. S.: Estimation of land surface temperature over the Tibetan Plateau using AVHRR and MODIS data, *Adv Atmos Sci*, 27, 1110-1118, 10.1007/s00376-009-9133-0, 2010.



- 850 Zhong, L., Ma, Y., Hu, Z., Fu, Y., Hu, Y., Wang, X., Cheng, M., and Ge, N.: Estimation of hourly land surface heat fluxes over the Tibetan Plateau by the combined use of geostationary and polar-orbiting satellites, *Atmospheric Chemistry and Physics*, 19, 5529-5541, 10.5194/acp-19-5529-2019, 2019a.
- Zhong, L., Zou, M., Ma, Y., Huang, Z., Xu, K., Wang, X., Ge, N., and Cheng, M.: Estimation of Downwelling Shortwave and Longwave Radiation in the Tibetan Plateau Under All-Sky Conditions,
- 855 *Journal of Geophysical Research: Atmospheres*, 124, 11086-11102, 10.1029/2019jd030763, 2019b.
- Zhou, Y., Li, Z., Li, J., Zhao, R., and Ding, X.: Glacier mass balance in the Qinghai–Tibet Plateau and its surroundings from the mid-1970s to 2000 based on Hexagon KH-9 and SRTM DEMs, *Remote Sensing of Environment*, 210, 96-112, 10.1016/j.rse.2018.03.020, 2018.

860